Paper

Int'l J. of Aeronautical & Space Sci. 16(2), 190–205 (2015)
DOI: http://dx.doi.org/10.5139/IJASS.2015.16.2.190

IJASS
International Journal of Aeronautical and Space Sciences

High-Velocity Impact Damage Behavior of Carbon/Epoxy Composite Laminates

Young A. Kim*

The 1st R&D Institute, Agency for Defense Development, Daejeon 305-152, Korea

Kyeongsik Woo**

School of Civil Engineering, Chungbuk National University, Cheongju, Chungbuk 360-763, Korea

Hyunjun Cho* and In-Gul Kim******

Department of Aerospace Engineering, Chungnam National University, Daejeon 305-764, Korea

Jong-Heon Kim*****

Airframe Technology Directorate, Agency for Defense Development, Daejeon 305-152, Korea

Abstract

In this paper, the impact damage behavior of USN-150B carbon/epoxy composite laminates subjected to high velocity impact was studied experimentally and numerically. Square composite laminates stacked with $[45/0/\text{-}45/90]_{ns}$ quasi-symmetric and $[0/90]_{ns}$ cross-ply stacking sequences and a conical shape projectile with steel core, copper skin and lead filler were considered. First high-velocity impact tests were conducted under various test conditions. Three tests were repeated under the same impact condition. Projectile velocity before and after penetration were measured by infrared ray sensors and magnetic sensors. High-speed camera shots and C-Scan images were also taken to measure the projectile velocities and to obtain the information on the damage shapes of the projectile and the laminate specimens. Next, the numerical simulation was performed using explicit finite element code LS-DYNA. Both the projectile and the composite laminate were modeled using three-dimensional solid elements. Residual velocity history of the impact projectile and the failure shape and extents of the laminates were predicted and systematically examined. The results of this study can provide the understanding on the penetration process of laminated composites during ballistic impact, as well as the damage amount and modes. These were thought to be utilized to predict the decrease of mechanical properties and also to help mitigate impact damage of composite structures.

Key words: High-Velocity Ballistic Impact, Composite Laminates, Impact Damage Mode and Extent, Residual Velocity

1. Introduction

Recently, there have been increased interests for use of composite materials. This is due to the advantageous mechanical properties that the composite materials can provide such as lightness and high specific strength and stiffness. Advanced composite materials have been used in the aerospace structures over the several decades, and the application is continuously expanding to defense, automotive, and sporting industries.

Laminated composite materials, however, have relatively low strength and stiffness in the thickness direction. As a result, the laminated composite materials are weak under transverse impact loading which is unavoidable in many

* Researcher
** Professor, Corresponding author: kw3235@chungbuk.ac.kr
*** Graduate student
**** Professor
***** Senior Researcher

Received: March 5, 2015 Revised: June 17, 2015 Accepted: June 24, 2015

http://ijass.org pISSN: 2093-274x eISSN: 2093-2480

practical applications. The composite materials also exhibit complicated failure behavior and the damage amount and mode are very difficult to define [1-2].

The aerospace structures are susceptible to impact damage by flying debris. Unlike metal, composite materials fail immediately without plastic deformation when loaded over the elastic limit. Though the mass of impact projectile may be comparatively small, the damage by high velocity impact can often be fatal. The mechanical properties of the damaged composite structures significantly decrease. Also if the impact accompanies penetration, it may threaten immediately major devices and explosive fuel tank, for instance, inside the structures. Therefore, it is important to understand the failure and penetration behavior of composite laminates under impact, as well as the structure failure and strength behavior after impact. Proper understanding of high-velocity impact damage extent and mode is one of the key elements for the establishment of structural integrity for aerospace structures, and thus, has been the focus of many researches over the past several decades [3-4].

The impact can be divided into low velocity and high velocity impact [3-8]. This classification depends not only on the projectile velocity but also on the material properties and the mass of the projectile, as well as the stiffness of composite laminates. In general, the impact velocity up to 10 m/s is classified as the low velocity impact and over 50 m/s velocity as the high velocity impact. The high velocity impact can be subdivided into medium (50 – 200 m/s), high (200 – 1,000 m/s), and hyper- or ultra-high velocity (1,000 m/s –) impact. Under low velocity impact, the global deformation is occurred throughout the structures. The impact damage is often hidden and cannot be detected by visual inspection. On the contrary, the damage by high velocity impact can be observed clearly. Not only the penetration path but also the locally large deformation near the impact site is clearly visible. Under high velocity impact, the kinematic energy of impact projectile is dissipated through several mechanisms. In this case, large deformation occurs locally at the impact site and various damage modes such as matrix cracking, fiber breakage, fiber/matrix debonding, delamination, perforation and etc. are involved. The resulting impact damage can significantly decrease the strength and stiffness of composite structures [9-11].

While the low velocity impact damage behavior of composite structures are relatively well studied (eg, refs. [6-8, 12]), a limited number of studies on the high velocity impact damage behavior have been reported. Due to the complexity of the microstructural failure modes, the studies have been performed mostly by experiments. However, the impact experiments are very costly and time consuming. Moreover, the results may be valid only for the tested configuration. Recently, numerical analysis has been applied to simulate the penetration velocity and the impact damage behavior [13-16]. Due to the continuous development of numerical algorithm and material models, the accuracy and the applicability of simulation results are increasing.

In this paper, the high velocity ballistic impact behavior of carbon/epoxy laminated composites was studied. The composite laminates were stacked by USN-150B carbon/epoxy laminas (SK chemicals, [17-18]) with the stacking sequences of $[45/0/-45/90]_{ns}$ and $[0/90]_{ns}$. The number of plies considered was 32, 48, 64, and 80. In the experiment, the conical shape projectiles of armor piercing shell and steel core ammunition were impacted on the center of the composite plates with the initial velocities of 600 m/s and 800 m/s. The initial and residual velocities were measured by infrared ray sensors and magnetic sensors. High-speed camera shots and C-scan images were also taken to estimate the projectile velocities and to obtain the information on the damage shapes of the projectile and the laminates. Next, finite element analyses were performed to simulate the impact experiments using commercial explicit nonlinear finite element code LS-DYNA (v. 971) [19]. Both composite laminates and projectile was modeled using three-dimensional elements with reduced integration. Continuum damage mechanics-based failure model MAT 59 was applied in FE simulation to predict the damage mode and extent. The analysis results were systematically investigated focusing on the prediction of residual velocity of the projectile and the damage extents and mode of the laminated composites.

2. Experiment

In this study, high velocity impact tests were performed for square shaped carbon/epoxy composite laminates with various thicknesses and sizes of the deformable section. Fig. 1 shows the configuration of the impact tests. The composite

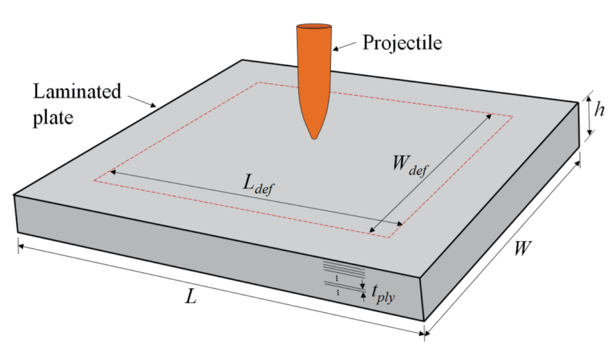

Fig. 1. Schematic configuration of composite laminates and projectile

laminates were made of USN-150B carbon/epoxy lamina (t_{ply}=0.141 mm). The composite laminate specimens have the stacking sequence of $[45/0/-45/90]_{ns}$. The number of layers (N_L) considered was 32 (n=4), 48 (n=6), 64 (n=8), and 80 (n=10) and the corresponding plate thicknesses (h) were 4.512 mm, 6.768 mm, 9.024 mm, and 11.28 mm, respectively. Composite laminate specimens with the stacking sequence of $[0/90]_{16s}$ with N_L=64 were also considered. The specimens were fabricated in 2 size sets. The width and length of the specimens was $L \times W$=87.5×87.5 mm² for specimens with N_L=32, 64, and 80, and $L \times W$=150×150 mm² for specimens with N_L=48. The sizes of the deformable section were $L_{def} \times W_{def}$=65×65 mm² for the first set, and $L_{def} \times W_{def}$=100×100 mm² with for the second set, respectively.

The upper and lower surfaces of specimen were clamped except the deformable region. The 150×150 mm-square steel plate jig with 65×65 mm-square cut-out (100×100 mm-square cut-out for the second set) was used to clamp the specimen with 1 steel toggle clamp on each side to represent the fixed boundary condition.

Figure 2 shows the cross-sectional view of the impact projectiles. Two types of impact projectiles were considered: steel core ammunition (*Projectile-HC*) and armor piercing shell (*Projectile-AP*). Both projectiles have basically the same structure consisting of steel core and copper skin, while the size of *Projectile-AP* is bigger. The skin thicknesses of the *Projectile-HC* and *Projectile-AP* were 0.69 mm and 0.785 mm, respectively. A small amount of lead was added in the head section between the core and the copper skin. The masses were 3.59 g for the *Projectile-HC* and 10.583 g for the *Projectile-AP*. The constituent masses were summarized in Table 1.

Figure 3 illustrates schematic diagram of ballistic impact gun facility which consisted of a firing gun, a projectile, a laminated composite specimen, a jig apparatus, a high speed camera, velocity measuring sensors, and DAQ system [18]. The specimen jig apparatus was carefully set-up to have right angle impacts on the center of the laminate specimens. Special care was performed to reduce the angle of squint. In the experiment, the impact projectiles were accelerated to the desired velocity by the firing gun. The initial velocity of the projectile was controlled by adjusting the amount of the gunpowder. In this study, the two impact velocities of approximately 600 m/s and 800 m/s were considered.

Three experiments per configuration were performed under the same impact condition. The projectile velocities before and after penetration were obtained by analyzing the high speed camera images. The high-speed camera

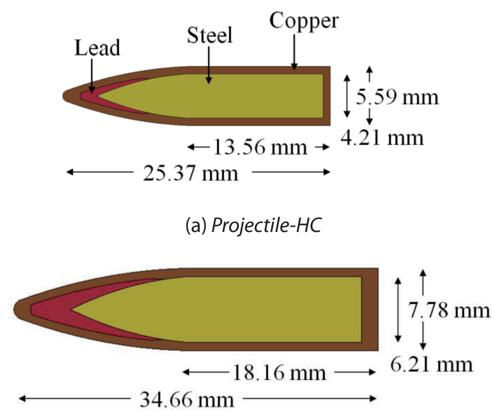

(a) *Projectile-HC*

(b) *Projectile-AP*

Fig. 2. Projectile configuration

Table 1. Projectile mass (unit=g)

	Projectile-HC	*Projectile-AP*
Steel	1.777	5.203
Copper	1.713	5.080
Lead	0.100	0.300
Total	3.590	10.583

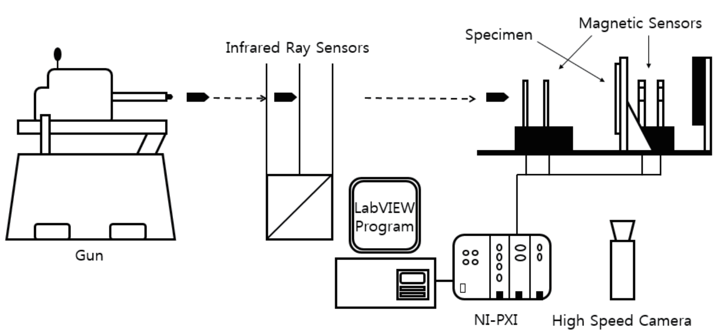

Fig. 3. Schematic diagram of ballistic impact test set-up

DOI: http://dx.doi.org/10.5139/IJASS.2015.16.2.190

also provided the information of the initial and residual velocities and the deformed/failed shape of the projectile before and after the penetration. In addition, three infrared ray sensors and four magnetic sensors were used to measure the velocities. The data obtained from the sensors were stored in a computer by NI-PXI device, which were then processed using LabVIEW program for further analysis and comparisons. The impactor velocities obtained by the high-speed camera image processing were fine-tuned with the velocities obtained by the latter methods, which were then considered as the experimental velocities.

3. Analysis

3.1 FE modeling

The high velocity impact tests were simulated using an explicit finite element code LS-DYNA [19]. Figure 4 shows the top view of the finite element mesh for $L \times W$=87.5×87.5 mm^2 laminated plate configuration with *Projectile-HC*. A radial type mesh refinement was used for the central portion of the laminate since an extensive failure was expected to occur in the region of the projectile path and in its surrounding region under high velocity impact. The finite element mesh for $L \times W$=150×150 mm^2 specimen configuration was made by adding additional elements to the outside region of the mesh for $L \times W$=87.5×87.5 mm^2. The mesh of the projectile was made refining in the nose cone portion to match the element size of the plate and also to model the curved geometry for accurate contact analysis.

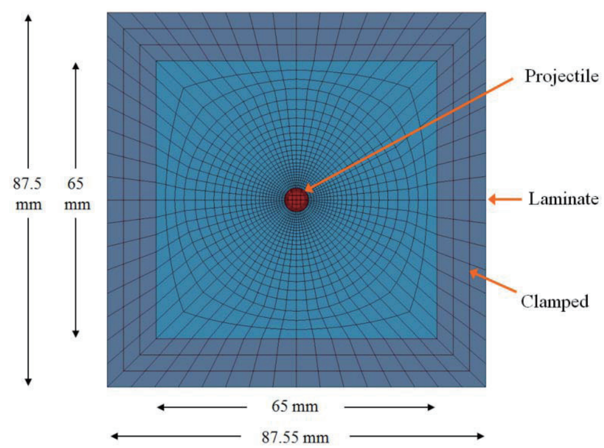

Fig. 4. Finite element model ($L \times W$=87.5×87.5 mm^2 laminate and *Projectile-HC*)

Both the projectile and the composite laminate were modeled using three-dimensional elements with reduced integration. The number of elements for the composite laminates and the projectiles was listed in Table 2. Each ply was modeled to have 1 element in the thickness direction. The number of elements per ply was 1,856 for $L \times W$=87.5×87.5 mm^2 specimen model and 2,240 for $L \times W$=150×150 mm^2 specimen model. Initially it appeared that the configuration was symmetric in the in-plane direction, and thus a quarter symmetry model could be used. However, the full model was used herein since the configuration would lose the symmetry once the impact failure and the element erosion would occur unsymmetrically.

The applied boundary condition was that all displacements of the upper and lower surface nodes outside the deformable region were constrained. For the projectile, the nodes along the center line were constrained to move in the vertical direction only.

Generally the use of elements with reduced integration in the high velocity impact analysis results in hourglass mode in which the internal energy is nearly zero although a large deformation occurs in the element. The hourglass mode may significantly affect the solution accuracy. The solution cannot be considered accurate when the hourglass energy exceeds more than 10% of the internal energy. The use of fully integrated elements does not involve the hourglass problem, but in this case the computation becomes inefficient due to the increase of computational cost. The hourglass problem can be controlled by either viscosity or stiffness type option

Table 2. Number of elements

(a) Laminated composite specimen

No. of layer (N_L)	32	48	64	80
87.5×87.5 mm^2 model	59,392	89,088	118,784	148,480
150×150 mm^2 model	71,680	107,520	143,360	179,200

(b) Projectile

	Projectile-HC	*Projectile-AP*
Steel	383	799
Copper	743	1,151
Lead	203	529

in LS-DYNA. In this study, the stiffness based hourglass control was employed.

For the contact between the impact projectile and the composite plate, ERODING_SURFACE_TO_SURFACE was used with penalty contact option in LS-DYNA. The static (S_{FRIC}) and dynamic friction coefficients (D_{FRIC}) used were 0.3 and 0.1, respectively. The finite elements of the composite plate were deleted when either the specified failure criterion was satisfied or the failure strain (FS) was reached the prescribed value for each material.

3.2 Material modeling

In this study, MAT59 (MAT_COMPOSITE_FAILURE_SOLID) was used for the composite laminates in LS-DYNA. This material model is an orthotropic material model which uses the maximum stress failure criterion for tension failure, compressive failure, shear failure and delamination. This material model has been used to simulate impact and crush simulations of thick composite structures with solid elements [20-22]. The failure criterion of this material model is given as follows [19, 23]. Each failure mode is classified according to the fiber direction. (Here, the subscripts 1, 2, and 3 denote the fiber, matrix, and transverse directions.)

(*F1*) Longitudinal tensile failure (σ_{11}>0)

$$\left(\frac{\sigma_{11}}{X_t}\right)^2+\left(\frac{\sigma_{12}}{S_{12}}\right)^2+\left(\frac{\sigma_{13}}{S_{13}}\right)^2 \geq 1.0 \tag{1}$$

(*F2*) Transverse tensile failure (σ_{22}>0)

$$\left(\frac{\sigma_{22}}{Y_t}\right)^2+\left(\frac{\sigma_{12}}{S_{12}}\right)^2+\left(\frac{\sigma_{23}}{S_{23}}\right)^2 \geq 1.0 \tag{2}$$

(*F3*) Through-thickness shear failure (longitudinal)

$$\left(\frac{\sigma_{11}}{X_t}\right)^2+\left(\frac{\sigma_{13}}{S_{13}}\right)^2 \geq 1.0 \tag{3}$$

(*F4*) Through-thickness shear failure (transverse)

$$\left(\frac{\sigma_{22}}{Y_t}\right)^2+\left(\frac{\sigma_{23}}{S_{23}}\right)^2 \geq 1.0 \tag{4}$$

(*F5*) Delamination failure (through-thickness tension, σ_{33}>0)

$$\left(\frac{\sigma_{33}}{Z_t}\right)^2+\left(\frac{\sigma_{13}}{S_{13}}\right)^2+\left(\frac{\sigma_{23}}{S_{23}}\right)^2 \geq 1.0 \tag{5}$$

(*F6*) Longitudinal compressive failure (σ_{11}<0)

$$\left(\frac{\sigma_{11}}{X_c}\right)^2 \geq 1.0 \tag{6}$$

(*F7*) Transverse compressive failure (σ_{22}<0)

$$\left(\frac{\sigma_{22}}{S_{12}+S_{23}}\right)^2+\left[\left(\frac{Y_c}{S_{12}+S_{23}}\right)^2-1\right]\frac{\sigma_{22}}{|Y_c|}^2+\left(\frac{\sigma_{13}}{S_{13}}\right)^2+\left(\frac{\sigma_{23}}{S_{23}}\right)^2 \geq 1.0 \tag{7}$$

(*F8*) Through-thickness compressive failure (σ_{33}<0)

$$\left(\frac{\sigma_{33}}{S_{13}+S_{23}}\right)^2+\left[\left(\frac{Z_c}{S_{13}+S_{23}}\right)^2-1\right]\frac{\sigma_{33}}{|Z_c|}+\left(\frac{\sigma_{13}}{S_{13}}\right)^2+\left(\frac{\sigma_{23}}{S_{23}}\right)^2 \geq 1.0^2 \tag{8}$$

When the failure criterion was met along a particular direction, the stiffness was set to zero in a time interval of 100 times steps. The above criteria were applied along with the failure criteria by limit of time step size, ultimate strain, and ultimate effective strain. The elements were counted as completely failed if the tension/compression strains or the effective strain were larger than the specified values, which were then deleted from the analysis.

The steel, copper and lead materials in the projectile were modeled using the material model MAT3 (MAT_PLASTIC_KINEMATIC) with bi-linear elastic-plastic stress-strain curves. This material model is known to be well suited to describe the elastic and plastic behavior as well as the failure behavior. The projectile elements having effective strain larger than the specified failure strain were also deleted from the analysis.

Properties for the composite lamina and the constituent materials of the impact projectiles were shown in Table 3. It is well known that the properties of composite materials exhibit a large amount of scattering. Also, these depend on the strain rate, and the rate dependence can be significant particularly when the impact velocity is very high (e.g., [24-25]). Although LS-DYNA has a material card to model the rate effect [13, 26], this requires dynamic test data for a wide range of loading rates for accurate consideration. In this study, a series of preliminary simulations were performed to select and fine tune the appropriate material properties that produced matched results compared to the experimental data. The rate dependence was accounted for by increasing material strength by 10%. It was also found in the preliminary analysis that unrealistically early failure initiation and propagation occurred due to compressive failure in the thickness direction. Therefore, the out-of-plane compressive failure was disregarded by assigning a large value for the compressive strength in the out-of-plane direction.

The failure parameters for the constituent materials of the projectile were also calibrated. The failure strain values for the copper skin and the lead filler materials were selected by performing analyses and then comparing the residual velocities and the failure shapes to those by the experiments. The failure strain of steel core material was set to zero in the analysis nullifying the failure because no failure was observed with only a small amount of deformation from the

Table 3. Material property

(a) Composite layer – USN 150B

Density (Ton/mm^3)	ρ	1.544x10^{-9}
Thickness (mm)	t_{ply}	0.141
Young's modulus (GPa)	E_{11}	131
	$E_{22} = E_{33}$	8
Poisson's ratio	$\nu_{12} = \nu_{13}$	0.018
	ν_{23}	0.47
Shear modulus (GPa)	$G_{12} = G_{13}$	4.5
	G_{23}	3.5
Tensile strength (MPa)	X_t	2,000
	$Y_t = Z_t$	61
Compressive strength (MPa)	X_c	2,000
	$Y_c = Z_c$	200
Shear strength (MPa)	$S_{12} = S_{13}$	70
	S_{23}	40

(b) Projectile – Steel 4340

Density (Ton/mm^3)	ρ	7.85x10^{-9}
Young's modulus (GPa)	E	210
Poisson's ratio (GPa)	ν	0.3

(c) Projectile – C2100

Density (Ton/mm^3)	ρ	8.86x10^{-9}
Young's modulus (GPa)	E	115
Poisson's ratio (GPa)	ν	0.307
Failure strain	FS	0.1

(d) Projectile – Lead

Density (Ton/mm^3)	ρ	10.22x10^{-9}
Young's modulus (GPa)	E	36
Poisson's ratio (GPa)	ν	0.42
Failure strain	FS	0.17

pictures taken by the high speed camera in the experiments.

4. Results and discussion

In this section, the failure behavior of carbon/epoxy laminated composite plates under high velocity impact is discussed. First, the impact penetration behavior was described, with the examination of the time history of the projectile velocity, followed by the comparison between the predicted and experimentally measure residual velocities. Next, the energy balance and the contact force history were examined. Finally the mode and extent of damage in the composite plates and the projectile were discussed. Tests and analyses were performed for $L \times W$=87.5×87.5 mm^2 and $L \times W$=150×150 mm^2 specimens with $[45/0/-45/90]_{ns}$ and $[0/90]_{ns}$ stacking sequences with the number of layers in the range between 32 – 80. Also, two types of projectiles (*Projectile-HC* and *Projectile-AP*) with impact velocities of approximately 600 m/s and 800 m/s were considered. The results were systematically examined focusing on those for $L \times W$=87.5×87.5 mm^2 specimens with $[45/0/-45/90]_{ns}$ stacking sequences. It should be noted that the experimental results were selectively chosen and presented herein for the comparison with those by the analyses since the repeatability of the experiment in getting the impact velocity close enough for example was practically not attainable.

4.1 Penetration process

Figure 5 shows the numerically predicted deformed shapes of the impact projectile and the laminated composite plate for 2 different time stages during the impact penetration for the 64-ply 87.5×87.5 mm[2] specimen configuration with $[45/0/\text{-}45/90]_{8s}$ stacking sequence. The impactor was *Projectile-HC* and the initial velocity (v_i) was 597.5 m/s. One half portion of the configuration was plotted to show the cross-sectional view.

As can be seen in the figure, at t=0.02 mili-seconds (ms) after the impact, the nose cone of the projectile entered well into the composite plate. The lead filler material of the projectile was almost fully failed and eroded, and the front portion of the copper skin was crushed and peeled off. The composite elements in the projectile penetration path failed and eroded. Also, the upper portion of the plate near the penetration region showed a large amount of local deformation, which resulted in shear failure and delamination.

At t=0.056 ms, the penetration was in the final stage. The elements of the composite plate at the penetration path were either eroded or detached from the main structure. The damaged area around the projectile path increased toward the projectile exiting side and the size of the damage at the bottom surface became much larger than that at the entering top surface. One can observe that at this high impact velocity, the damage deformation of the composite plate was localized around the projectile path. Away from that region, negligibly small global plate deformation occurred. A large amount of damage occurred in the projectile also. The elements of the lead material were completely deleted and the whole elements of the front cone section of the copper skin material were eroded. The projectile exited at about t = 0.065 ms and the residual velocity (v_r) of the projectile predicted by the analysis for this case was 538.2 m/s.

4.2 Residual velocity and contact force history

The predicted velocity time histories of the *Projectile-HC* impacted on the 87.5×87.5 mm[2] composite specimens stacked with 32-, 64- and 80-ply $[45/0/\text{-}45/90]_{ns}$ laminates are shown in Fig. 6. The initial impact velocities for the cases shown in the figure were approximately 600 m/s. The velocity curves plotted were the traced values at a center node of the projectile steel core. The velocity of the projectile decreased quickly after the projectile contacted with and penetrated through the laminates. Once the penetration was completed the projectile velocity became almost constant. One can observe that the velocity curves exhibited a large amount of oscillation. This was due to the vibration of the deformable projectile body in the axial direction, and also due to the continued hitting of the projectile to the flying debris after the projectile penetrated through the plate. As expected, the cases with thicker laminates resulted in the smaller residual velocities.

The contact force histories between the projectile and the composite plate are shown in Fig. 7, which were also highly oscillatory. At the beginning of the penetration, the contact force history was similar regardless of the number of plies. However, different force history was obtained as the

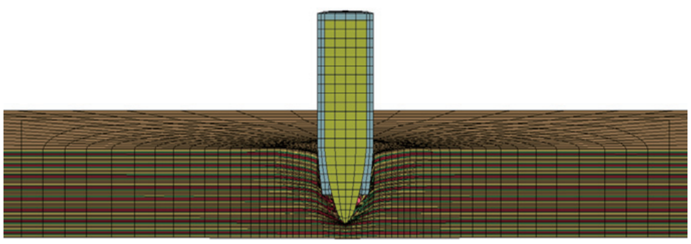

(a) t=0.02 ms

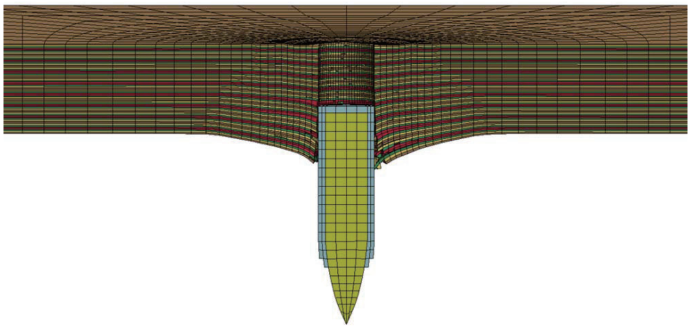

(b) t=0.056 ms

Fig. 5. Penetration process of 87.5×87.5 mm^2 $[45/0/\text{-}45/90]_{8s}$ laminate impacted by *Projectile-HC* (v_i=597.5 m/s)

penetration progressed. As the number of plies increased, the peak contact force increased and the time to the peak value delayed. The peak contact force occurred at around t=0.014 ms, 0.021 ms, and 0.024 ms for the cases with the number of plies N_L=32, 64, and 80, respectively. In general, the peak contact force value occurred approximately just before the front nose cone part of the projectile penetrated the last layer of the laminate. After that the contact force decreased and became negligibly small once the nose cone part exited from the composite plate.

Table 4 compares the numerically predicted residual velocities with those measured by experiments. The experimental impact and residual velocities were the averaged values of 3 experiments for each case. The predicted residual velocities were obtained by averaging the time history values of the projectile velocity over the 0.05 ms after the projectile exiting time point. In general, the predicted residual velocities of the projectiles agreed well to those obtained by the experiments. Here, the relative differences, defined as (numerical v_r – experimental v_r)/(experimental v_r), were small for all considered cases. The maximum relative difference was only 6.83%. Better agreements were found for the cases impacted by the *Projectile-HC* than those impacted by the *Projectile-AP*.

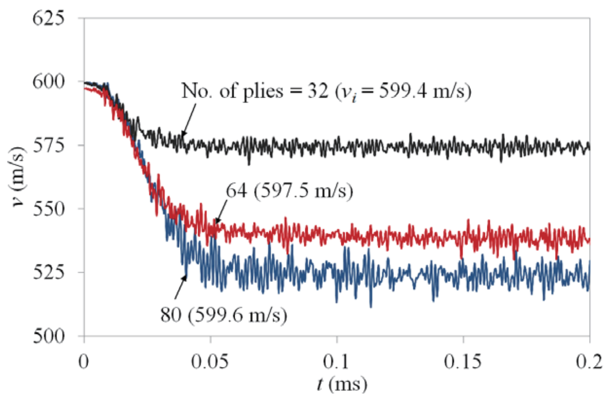

Fig. 6. Velocity time history of *Projectile-HC* impacted on 87.5 × 87.5 mm² [45/0/-45/90]$_{ns}$ laminates

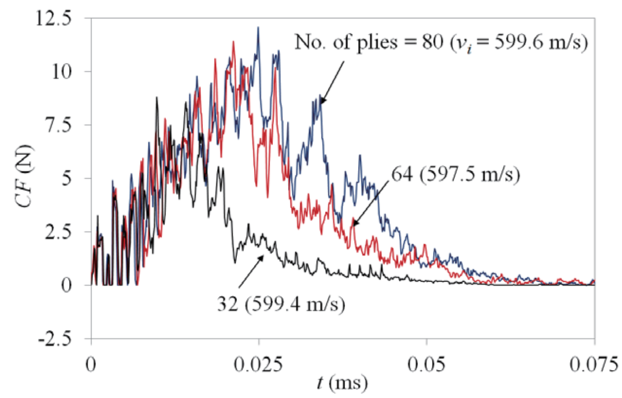

Fig. 7. Time history of contact force for 87.5 × 87.5 mm² [45/0/-45/90]ns laminates impacted by *Projectile-HC*

Table 4. Comparison of the residual velocities of projectiles

(a) *Projectile – HC*

Stacking Sequence	Specimen Size (mm²)	No. of Plies	Impact Velocity (v_i, m/s)	Residual Velocity (v_r, m/s) Experiment	Analysis	Difference (%)
[45/0/-45/90]$_{NS}$	150×150	48	616.8	565.4	580.11	2.60
		48	796.7	745.3	762.68	2.33
	87.5×87.5	32	599.4	570.6	574.11	0.62
		64	597.5	520.4	538.20	3.42
		64	809.5	771	764.7	-0.82
		80	599.6	539.7	523.76	-2.95
[0/90]$_{NS}$		64	616.8	527.8	563.83	6.83

(b) *Projectile – AP*

Stacking Sequence	Specimen Size (mm²)	No. of Plies	Impact Velocity (v_i, m/s)	Residual Velocity (v_r, m/s) Experiment	Analysis	Difference (%)
[45/0/-45/90]$_{NS}$	150×150	48	603.6	553.7	578	4.39
		48	804.9	737.8	785.15	6.42
	87.5×87.5	32	803.9	753.7	790.17	4.84
		64	581.7	529.5	547.47	3.39
		64	794.3	741.3	766.45	3.39
		80	779.7	729.4	745.91	2.26
[0/90]$_{NS}$		64	793.2	740.3	764.98	3.33

The amount of change in the projectile velocity before and after the impact penetration was plotted in Fig. 8. The velocity decrease (Δv) was defined as the difference between the initial velocity and the residual velocity and related to the amount of the consumed energy during the penetration. The dash and dash-dot lines are the fitted curves for the cases with the $v_i \approx 600$ m/s and 800 m/s, respectively. As expected the thicker the composite laminates became, the larger the velocity of the projectile decreased. Also, the *Projectile-HC* had the larger velocity decrease since with the lighter mass it was required to have the larger velocity difference to consume the same amount of kinetic energy than the heavier *Projectile-AP*. For the configurations with the same thicknesses, the velocity decrease was larger when the impact velocity was around 600 m/s than 800 m/s, which was understandable similarly.

4.3 Mass variation

Figure 9 compares the experimental and analytical failure shape of the projectile impacted on the 64-ply 87.5×87.5

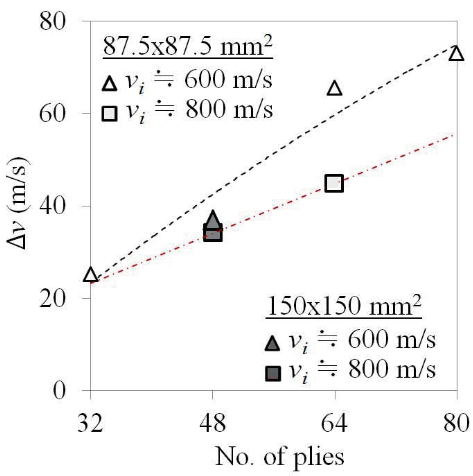

(a) *Projectile-HC*

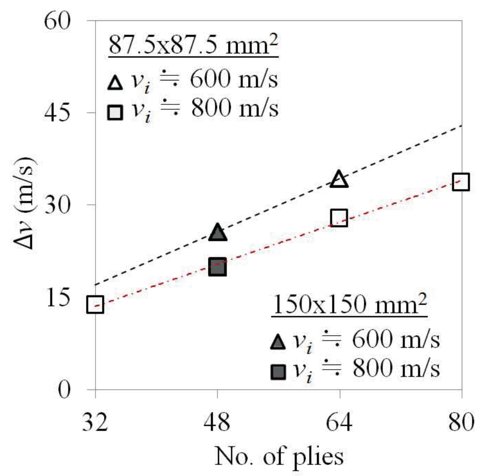

(b) *Projectile-AP*

Fig. 8. Velocity decrease for configurations with $[45/0/-45/90]_{ns}$ stacking sequence

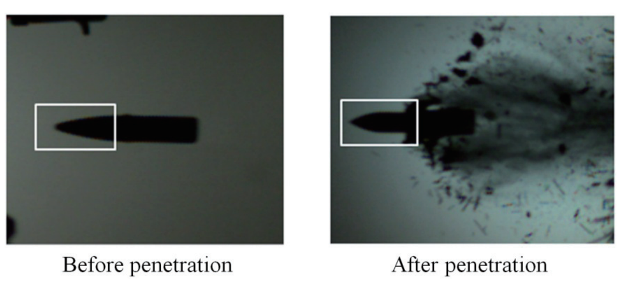

(a) Experiment – *Projectile-HC* (v_i=597.5 m/s)

(b) Analysis – *Projectile-HC* (v_i=597.5 m/s)

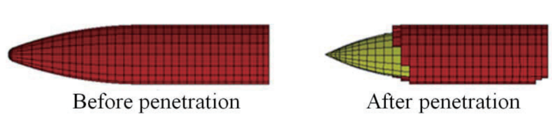

(c) Analysis – *Projectile-AP* (v_i=581.7 m/s).

Fig. 9. Damage shape of projectiles impacted at 87.5×87.5 mm^2 $[45/0/-45/90]_{8s}$ laminates

mm² laminated composite plate with $[45/0/-45/90]_{8s}$ stacking sequence with the initial velocity v_i=597.5 m/s for the *Projectile-HC* and 581.7 m/s for the *Projectile-AP*, respectively. In Fig. 6(a) which shows the high speed camera shots before and after the penetration for the *Projectile-HC*, one can clearly observe that the front portion of the projectile was peeled off while the steel core was in-tact with the original conical shape being kept after the penetration. The numerically predicted final shape of the *Projectile-HC* is shown in Fig. 6(b), which matched reasonably well to the shape obtained by the experiment. The final mesh of the *Projectile-AP* with v_i=581.7 m/s was plotted in Fig. 6(c) which showed a little bit more peeled-off damage shape of the nose cone skin.

Table 5 compares the projectile mass after penetration obtained by the experiments and the analyses. The experimental projectile mass after penetration was estimated from the pictures taken by the high speed camera since the mass data were not attainable from the collected projectiles afterward which were either completely disintegrated or severely damaged by the capturing apparatus. The numerically predicted mass was calculated from the elements excluding the ones eroded and flown away as debris. The table shows that the experimentally estimated and numerically predicted projectile mass change results agreed well. The difference in the mass change relative to the original mass was less than 7% for the *Projectile-HC*. For the *Projectile-AP*, a large scattering occurred in the experimentally estimated mass data. This was due to the non-uniform erosion as can be seen in Fig. 9(c) for the *Projectile-AP* which made the lost mass estimation from the high speed camera pictures less accurate. This resulted in larger relative difference between the experimentally estimated and the numerically predicted mass. Also, much larger mass change was resulted in for the cases with the *Projectile-AP* than those with the *Projectile-HC*. This was thought to be due to the larger size and the larger kinetic energy of the *Projectile-AP*. However, no strong dependence of the lost mass on the impact velocity, the number of plies, or the stacking sequence of the laminated composite plate was found.

The lost mass of the composite laminates by the impact was also examined. Fig. 10 shows the variation of the lost mass versus the laminate thickness predicted by the analysis. The lost mass was calculated by adding the mass of the eroded elements and the flown-off debris elements. The experimental results were not plotted since the measured mass of the laminate specimens after the impact did not differ enough from the original mass to determine the value of the lost mass. Here, the dashed line indicates the estimated lost mass assuming that only the portion of the laminates in the projectile path was lost. For all cases, the predicted lost mass was slightly larger than the mass in the projectile path. The laminates impacted by the larger and heavier *Projectile–AP* had larger lost mass than those impacted by the smaller

Table 5. Comparison of projectile mass after penetration

(a) *Projectile – HC* (Initial mass = 3.59 g)

Stacking Sequence	Specimen Size (mm²)	No. of Plies	Impact Velocity (v_i, m/s)	Projectile Mass		
				Experiment (g)	Analysis (g)	Difference (%)
$[45/0/-45/90]_{NS}$	150×150	48	616.8	3.28	3.22	1.67
		48	796.7	3.24	3.2	1.11
	87.5×87.5	32	599.4	3.05	3.29	-6.69
		64	597.5	3.05	3.07	-0.56
		64	809.5	2.93	3.02	-2.51
		80	599.6	3.08	2.92	4.46
$[0/90]_{16S}$		64	616.8	2.98	3.2	-6.13

(b) *Projectile – AP* (Initial mass = 10.583 g)

Stacking Sequence	Specimen Size (mm²)	No. of Plies	Impact Velocity (v_i, m/s)	Projectile Mass		
				Experiment (g)	Analysis (g)	Difference (%)
$[45/0/-45/90]_{NS}$	150×150	48	603.6	8.47	9.47	-9.45
		48	804.9	8.72	9.68	-9.07
	87.5×87.5	32	803.9	10.58	9.91	6.36
		64	581.7	6.95	9.12	-20.50
		64	794.3	8.37	8.91	-5.10
		80	779.7	7.33	8.49	-10.96
$[0/90]_{16S}$		64	793.2	8.34	9.06	-6.80

and lighter *Projectile-HC*. As the number of plies increased, the predicted lost mass tended to deviate from the linear dashed line which was thought to be related to the larger damage in the exit side of the thicker laminates. However, as in the case of the lost mass of the projectile, the dependency of the lost mass of the laminates on the impact velocity, the stacking sequence, and even the size of the specimen of the laminated composite plate was found not significant in the considered impact velocity range.

4.4 Energy balance

During the impact penetration, the kinetic energy of the projectile is consumed by various mechanisms. Fig. 11 shows the time histories of energy. As can be seen in the figure, as soon as the contact between the projectile and the composite plate started the kinetic energy (*KE*) rapidly decreased while the internal energy (*IE*), hourglass energy (*HGE*), sliding energy (*SLE*), eroded kinetic energy (KE^{eroded}), and eroded internal energy (IE^{eroded}) increased. The rate of the energy variation decreased as the penetration process progressed and became almost constant after the projectile exited the composite plate, as was the velocity time history in Fig. 6. Due to the very high initial and residual impactor velocities, the residual kinetic energy was still very high compared to other energy.

The eroded kinetic energy consisted of the kinetic energy of the eroded nodes of both the composite laminate and the projectile. In fact, the eroded kinetic energy was the largest energy consumer since the elements of the copper skin and the lead filler in the nose cone portion with very high kinetic were eroded. The sliding energy occurred by the friction between the projectile and the composite laminate during the penetration (D_{FRIC}=0.1) was the next major energy consumer, and the energy was also consumed by the eroded internal energy of the deleted elements. In this study, hourglass type 4 was used with default values to control the zero energy mode

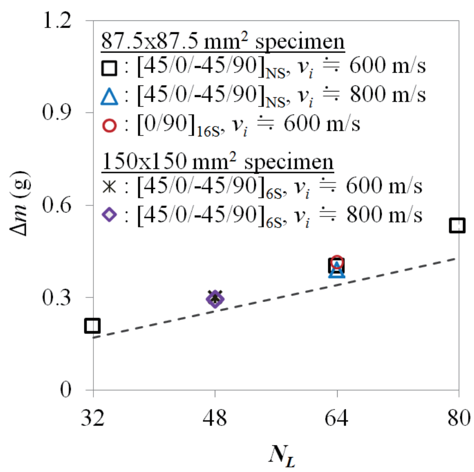

(a) *Projectile-HC*

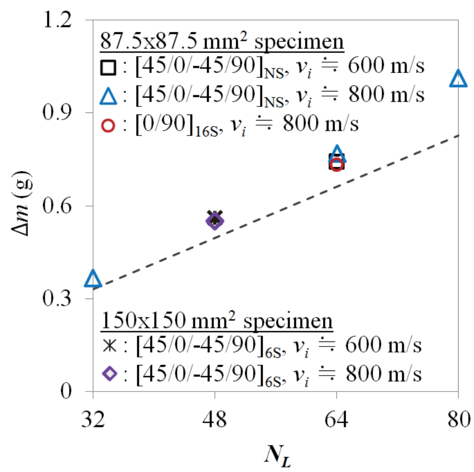

(b) *Projectile-AP*

Fig. 10. Lost mass of composite laminates by the impact

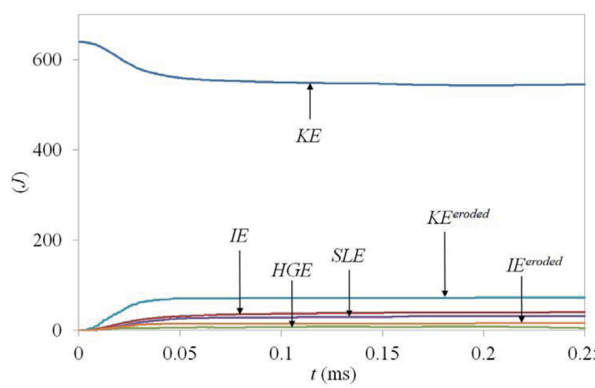

Fig. 11. Global energy balance of 87.5×87.5 mm² $[45/0/-45/90]_{8s}$ laminate impacted by *Projectile-HC* (v_i=597.5 m/s)

deformation. In the figure, the level of the artificial hourglass energy remained relatively small compared to others which ensured the accuracy of the analysis.

4.5 Failure mode and extent

Failure mode and range of composite laminates by the penetration was investigated in this study. MAT59 provides 8 failure modes in eqs. (1)-(8). As discussed earlier, the use of nominal value of Z_c in eq. (8) predicted unrealistically early failure initiation, and thus, the compressive failure mode in the through-thickness direction (*F8*) was thought to be under-predicted since only the shear stress was set to contribute to this mode. Also, it was found from preliminary analyses that the predicted delamination failure (*F5*) was surprisingly negligible. This was because of the limitation of the used material model which might not be able to predict the delamination failure correctly [16]. It was suggested that the through-thickness transverse shear failure might be predicted to occur beforehand and obviate the prediction of the delamination failure for the current problem.

Figure 12 shows the cross-sectional view of the failure maps for the 87.5×87.5 mm² $[45/0/\text{-}45/90]_{8s}$ laminate impacted by the *Projectile-HC* with the initial velocity of 597.5 m/s. The figures were plotted for the deformable region of the laminate (65×65 mm²). The color code of '1' indicates undamaged pristine state while '0' indicates completely damaged state. In the figure, D_P^{hc} denotes the penetration diameter impacted by *Projectile-HC*. For the case shown here, the D_P^{hc} obtained by the simulation was 5.59 mm which was approximately the same as the diameter of the impact projectile. As can be seen in the figure, the transverse tensile (*F2*) and the through-thickness shear in transverse direction (*F4*) were the major failure modes for the current problems. The delamination failure (*F5*) and the through-thickness compressive failure (*F8*) were negligible, as discussed previously. Other failure modes were found to be limited to the relatively small area near the penetration path other than the total failure along the projectile penetration path. For both *F2* and *F4*, large amount of damage was observed in all plies, while particularly large damaged area was resulted in the plies toward the projectile exiting bottom surface.

In Fig. 12, more failure occurred toward the projectile exit surface. This can also be observed in Fig. 13 where the top views of *F2* failure and *F4* failure maps for the 4 plies at the projectile entry and exit surfaces were plotted. (Here, the ply number 1 is the ply at the projectile exit surface.) The white colored region at the central part indicates the projectile penetration hole. As can be seen in the figure, much wider region was failed in the plies located near the exit surface. This was because the region surrounding the projectile path of the plies toward the exiting side was pushed by the projectile as well as the failed laminate material which resulted in, in particular, the larger *F4* damaged area in the bottom plies near the projectile exit surface. One can also observe that the damage shape was non-symmetric with respect to the fiber orientation direction. This trend was more distinct for the transverse tensile failure mode and at the plies near the projectile exit surface. In Fig. 13(a), larger *F2* damage area tended to occur in the transverse direction to the local fiber directions. The effect of fiber orientation angle to the damage shape was not clear for the *F4* damage while much larger area was damaged. The small transverse tensile strength value (Y_c) was the main cause of the antisymmetric-like *F2* damage shape. The non-symmetric shape in the *F4* damage was thought to be because the initially symmetric stacking of the laminate and the symmetric shape of the

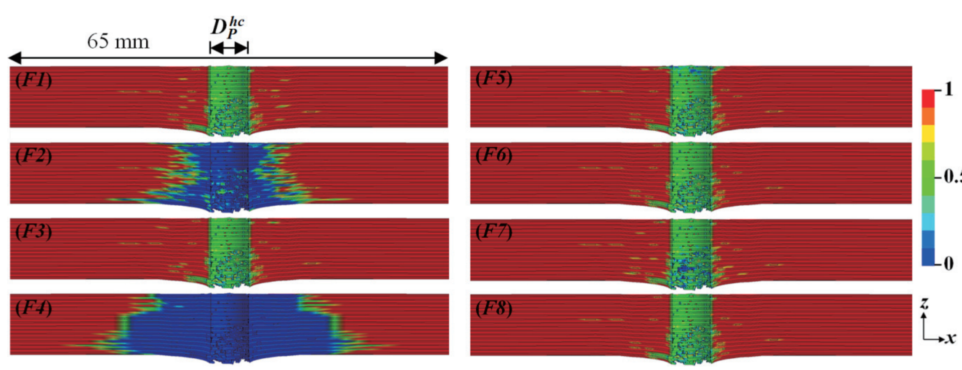

Fig. 12. Cross-sectional failure maps ($[45/0/\text{-}45/90]_{8s}$, v_i=597.5 m/s)

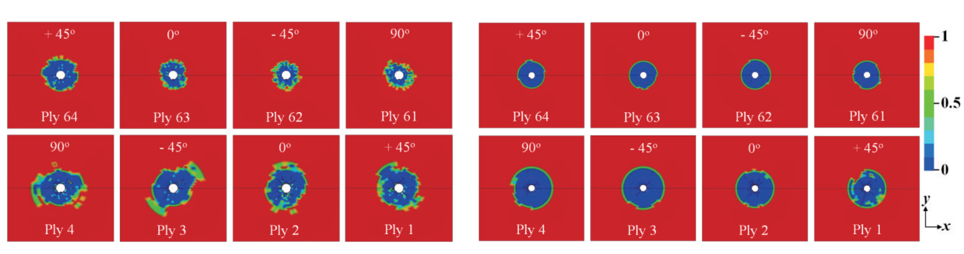

(a) Transverse tensile (*F2*) (b) Through-thickness transverse shear (*F4*)

Fig. 13. Failure maps at the top and bottom plies ($[45/0/\text{-}45/90]_{8s}$, v_i=597.5 m/s)

projectile became non-symmetric due to continuously non-uniform failure during the penetration process.

The maximum damage diameters of *F2* (D_2^{max}) and *F4* (D_4^{max}) estimated for the 87.5×87.5 mm² $[45/0/\text{-}45/90]_{8s}$ laminate impacted by the *Projectile-HC* with the initial velocity of 597.5 m/s were approximately 38.9 mm and 52.1 mm, respectively. The maximum damage diameters of the *F4* failure mode for the 32 ply- and 80 ply-laminates impacted by the *Projectile-HC* with v_i=599.4 m/s and 599.6 m/s were predicted to be 40.1 mm and 51.6 mm, respectively.

The damage extent was measured from the experimental specimens. Fig. 14 shows the ultrasonic C-scan image for 32-ply and 64-ply laminates impacted by *Projectile-HC* with impact velocities of with v_i=599.4 m/s and 597.5 m/s, respectively. The damage modes obtained from the C-scan image were the mixed ones but mostly by that of the delamination. The measured damage diameters were approximately 39 mm for the 32-ply laminate and 60 mm for the 64-ply laminate. The latter one was almost same as the specimen's deformable size, indicating that the damage propagated near to the gripped region of the laminate. Comparing the delamination damage extent obtained by the experiment and the numerically predicted *F4* damage extent, the analysis produced reasonably good results. (See the previous argument for the reason that this mode was used instead of delamination for comparison.) The damage size was only 2.8% different for the 32-ply laminate, while the damage size by the analysis was 14% smaller than that by the experiment for the 64-ply. This was thought to be partly due to the non-zero deformation of the grip device. While the grip made of steel plate was deformable in reality, it was assumed rigid in the analysis and all displacements were constrained for nodes at the grip region. The deformability of the grip seemed to affect the deformation in the grip region, in particular when the stiffness of the specimen was not small compared to that of the grip, resulting in larger delamination propagation.

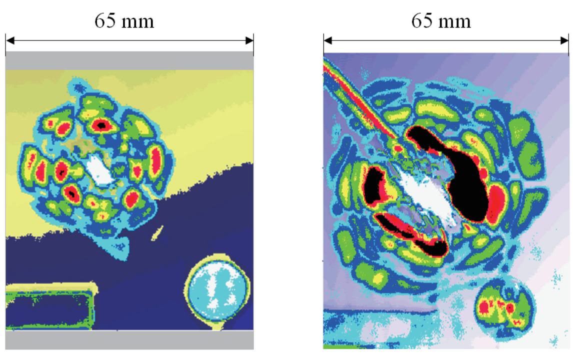

(a) 32 ply (v_i=599.4 m/s) (b) 64 ply (v_i=597.5 m/s)

Fig. 14. Ultrasonic C-scan image after impact

4.6 Through-the-thickness variation of damage

The through-thickness transverse shear failure (*F4*) was predicted as the major damage mode having the largest failed area, and was investigated further in detail. Fig. 15 shows the cross-sectional view of the *F4* failure distribution when the number of plies (N_L) was 32 and 80. (See Fig. 12 for the *F4* failure distribution for N_L=64.) Here, the stacking sequence was $[45/0/\text{-}45/90]_{ns}$ and impacted by *projectile-HC* with the initial velocity of approximately 600 m/s. Comparing these figures, one can see that the through-the-thickness distribution of the *F4* failure depended strongly on the number of plies of the composite laminates. For the 32-ply laminate, the amount of the *F4* failure was nearly uniform, while it was not for the 64-ply and 80-ply laminates. The thickness-wise variation was particularly significant when N_L=80 which had a much larger failure amount at the projectile exit side than that at the entry side of the laminate.

Figure 16 shows the *F4* failure shape for four plies at the projectile entry and exit sides. (See Fig. 13(b) for the *F4* failure shape when N_L=64.) In the figure, one can see that the failure area varied according to its location with respect to the impact direction as well as the orientation angle. The location dependence was clearly exhibited in the 80-ply laminate that had a much larger *F4* failure area in the exit side plies than that in the entry side plies. For the 32-ply

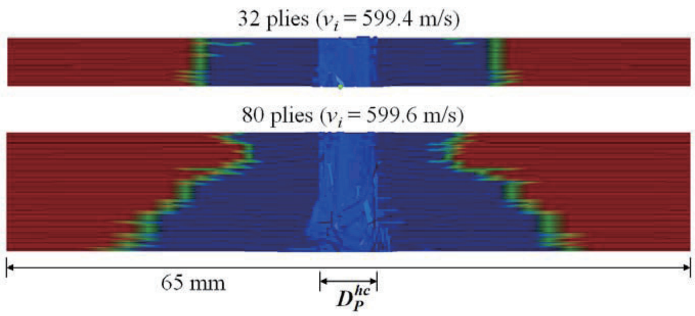

Fig. 15. Cross-sectional view of through-thickness transverse shear failure (*F4*) maps 32-ply and 80-ply laminates ($[45/0/\text{-}45/90]_{ns}$)

laminate, however, the variation was relatively small, only to be attributed to the orientation angle rather than to the thickness-wise location.

To examine the variation of the *F4* damage in the thickness direction, damage diameter (D_4) and damage non-uniformity (ΔD) for each ply are defined respectively as

$$D_4 \ = \frac{D_4^{max} + D_4^{min}}{2} \tag{9}$$

$$\Delta D = D_4^{max} - D_4^{min} \tag{10}$$

where D_4^{min} and D_4^{min} are the maximum and minimum *F4* damage diameters. The damage non-uniformity is defined as the difference between the maximum and minimum failure diameter for each ply and represents the degree of non-uniformity of the damaged area in the circumferential direction. Small values of ΔD indicate the damage has occurred relatively uniformly in the radial direction and the failed shape is nearly circular. The average damage diameter of the laminate is then defined as

$$\overline{D}_4 \ = (\textstyle\sum D_4)/N_{plies} \tag{11}$$

Figure 17 shows the distribution of the damage diameter and the non-uniformity for 32-ply, 64-ply, and 80-ply laminates impacted by *Projectile-HC* with the initial

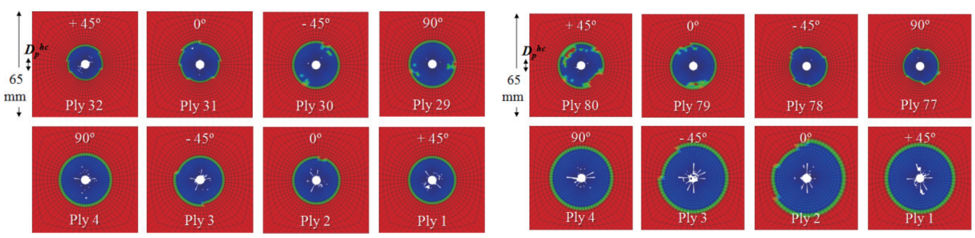

(a) 32 plies (b) 80 plies

Fig. 16. Through-thickness transverse shear failure (*F4*) map at the plies near the projectile entry and exit surfaces ([45/0/-45/90]$_{ns}$, v_i≒600 m/s)

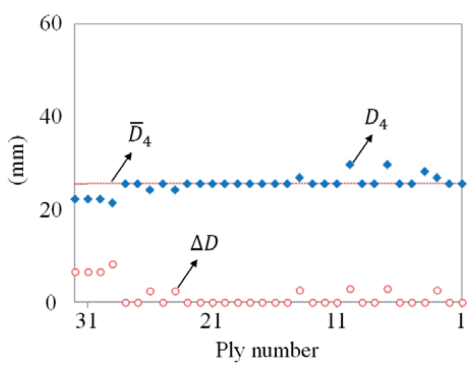

(a) N_L=32 (v_i=599.4 m/s)

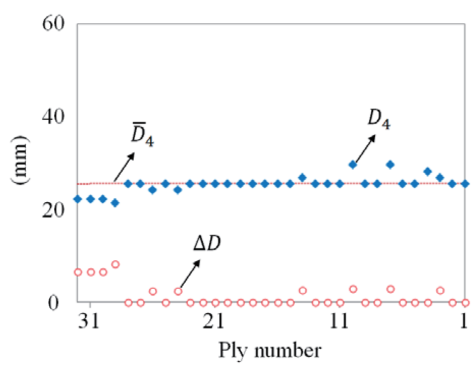

(b) N_L=64 (v_i=597.5 m/s)

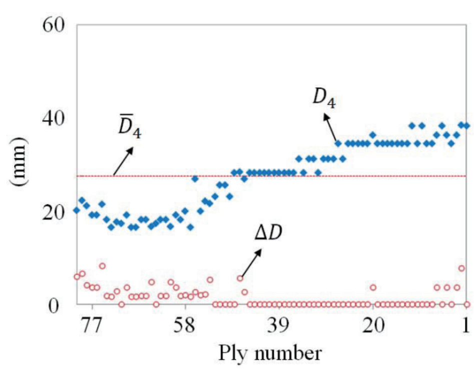

(c) N_L=80 (v_i=599.6 m/s)

Fig. 17. Through-thickness variation of *F4* damage diameter

velocity of approximately 600 m/s. In the figure, the dotted lines are the average damage diameters. All three laminates with different thicknesses showed similar average damage diameter values which are approximately 40% of the size of the deformable part. The ply damage diameter (D_4) for the 32-ply laminate did not vary much while it varied significantly for the 80-ply laminate. The larger damage size toward the projectile exiting surface (ply 1) can be observed clearly for the 80-ply laminate. The variation trend for the 64-ply laminate was between those of the 32-ply and the 84-ply laminates. The non-uniformity values (ΔD) were large at the plies near the entry and exit surfaces while they were relatively small at the mid-plies, indicating the damage shape was non-uniform at the outer plies and relatively uniform in the plies located inside. This, in turn, suggests that the effect of stacking sequence on the damage shape is large at the outer surfaces and small inside since the non-uniform damage shape is mainly caused by the change in the orientation angle.

The impact velocity also affected on the variation of ply damage diameters. In Fig. 17(b), when the impact velocity was 597.5 m/s, the size of the *F4* damage varied in the thickness direction, exhibiting that the ply damage size was smaller in plies near the entry surface and larger in plies near the exit surface. However, the variation trend when the impact velocity was 809.5 m/s as seen in Fig.18 was completely different. The damage size was almost equal in all plies and the average damage diameter was smaller than that with the impact velocity of 597.5 m/s. The variation was similar to the 32-ply laminate with the impact velocity of 599.4 m/s. From these results, it was thought that the damage size and shape were related to the relative thickness with respect to the impact velocity. At higher impact velocity, the through-thickness variation, the shape non-uniformity index, and the average diameter of damage decreased.

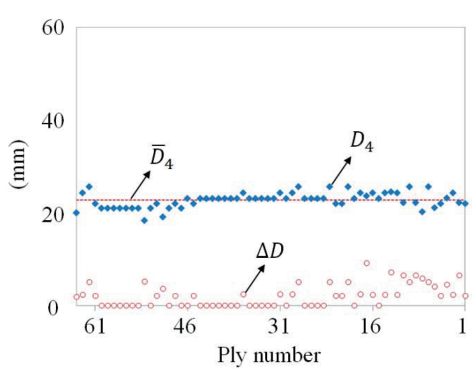

Fig. 18. Through-thickness variation of *F4* damage diameters for 64-ply laminates for v_i=809.5 m/s

5. Conclusion

In this study, the ballistic impact damage behavior of square $[45/0/-45/90]_{ns}$ quasi-isotropic and $[0/90]_{ns}$ cross-ply carbon/epoxy composite laminates was studied experimentally and numerically. Various laminate configurations with different thicknesses, two different types of conical projectiles and impact velocities of approximately 600 m/s and 800 m/s were considered. In the experiment, the projectile velocities before and after penetration were measured by infrared ray sensors and magnetic sensors. High-speed camera shots were also taken to provide the information of the projectile velocities and the deformed shape of projectiles. Damage extents of the specimens were measured by using C-Scan image. The numerical analysis was performed using explicit finite element code LS-DYNA. In the analysis, laminate specimens were modeled using solid elements with MAT 59, from which 8 failure modes were predicted. The projectile with steel core and copper skin were also discretely modeled using solid elements with MAT 3.

The experimental and numerical results agreed well. The residual velocities and the failure shape of projectile predicted by the numerical analysis matched reasonably well to those by the experiment, while the analysis under-predicted the failure size. The analysis results were examined focusing on the failure mode and the size of the failure. It was found that, other than the total failure in the projectile penetration path, the transverse tensile failure and the delamination failure were the dominant failure modes. The thickness and the impact velocity were also found to play a major role determining the circumferential and through-thickness variation of failure. The thicker laminate impacted by the slower projectile had the larger through-thickness variation with larger failure size toward bottom ply, while it was smaller for the thinner laminate impacted by the faster projectile. The circumferential delamination shape was non-uniform at the outer plies, while it was relatively uniform in the mid-plies

Acknowledgement

This work was supported by the Agency for Defense Development (ADD-13-01-08-23).

References

[1] Davies, G.A.O. and Zhang, X., "Impact Damage Prediction in Carbon Composites Structures," *Int. J. of Impact Engineering*, Vol. 16, No. 1, 1995, pp. 149-170.

DOI:10.1016/0734-743X(94)00039-Y

[2] Hou, J.P., Petrinic, N., Ruiz, C. and Hallett, S.R., "Prediction of Impact Damage in Composite Plates", *Composite Science and Technology*, Vol. 60, 2000, pp. 273-281.

DOI:10.1016/S0266-3538(99)00126-8

[3] Abrate, S., "Impact on Laminated Composite Materials," *Applied Mechanics Reviews*, Vol. 44, No. 4, 1991, pp. 155-190.

[4] Abrate, S., "Impact on Laminated Composites: Recent Advances," *Applied Mechanics Reviews*, Vol.47, No. 11, 1994, pp. 517-543.

DOI:10.1115/1.3111065

[5] Cantwell, W.J. and Morton, J., "Comparison of the Low and High Velocity Impact Response of CFRP," *Composites*, Vol. 20, Issue 6, 1989, pp. 545-551.

DOI:10.1016/0010-4361(89)90913-0

[6] Cantwell, W.J. and Morton, J., "The Impact Resistance of Composite Materials – A Review," *Composites*, Vol. 22, Issue 5, 1991, pp. 347-362.

DOI:10.1016/0010-4361(91)90549-V

[7] Richardson, M.O.W. and Wisheart, M.J., "Review of low-velocity impact properties of composite materials," *Composite Part A*, Vol.27, 1996, pp. 1123-1131.

DOI:10.1016/1359-835X(96)00074-7

[8] Agarwal, S., Singh, K.K. and Sarkar, P.K., "Impact Damage on Fibre-reinforced Polymer Matrix Composite – A Review," *J. of Composite Materials*, Vol. 48, No. 3, 2014, pp. 317-332.

DOI: 10.1177/0021998312472217

[9] Lee S. -W. R and Sun C. T, "Dynamic Penetration of Graphite/Epoxy Laminates by a Blunt-ended Projectile", *Composite Science and Technology*, Vol. 49, 1993, pp. 561-588.

DOI:10.1016/0266-3538(93)90069-S

[10] Morye S.S., Hine, P.J., Duckett, R.A., Carr, D.J. and Ward, I.M., "Modeling of the Energy Absorption by Polymer Composites under Ballistic Impact," *Composite Science and Technology*, Vol. 60, Issue 14, 2000, pp. 2631-2642.

DOI:10.1016/S0266-3538(00)00139-1

[11] Cheeseman, B.A. and Bogetti, T.A., "Ballistic Impact into Fabric and Compliant Composite Laminates", *Composite Structures*, Vol. 61, Issues 1-2, 2003, pp. 161-173.

DOI:10.1016/S0263-8223(03)00029-1

[12] Choi, H.Y. and Chang, F.K., "Impact Damage Threshold of Laminated Composites," *Applied Mechanics Division*, Vol.107, 1990, pp. 31-35.

DOI: 10.1177/002199839202601408

[13] Yen, C.-F., "Ballistic Impact Modeling of Composite Materials", *9th Int. LS-DYNA Conf.*, 2002.

[14] Loikkanen, M.J., "A Computational and Experimental Analysis of Ballistic Impact to Sheet Metal Aircraft Strictures," *9th European LS-DYNA Conf.*, 2005.

[15] Silva, M.A.G., Cismasiu, C. and Chiorean, C.G., "Numerical Simulation of Ballistic Impact on Composite Laminates", *Int. J. of Impact Engineering*, Vol.31, 2005, pp. 289-306.

DOI:10.1016/j.ijimpeng.2004.01.011

[16] Deka, L.J., Bartus,S.D. and Vaidya, U.K., "Damage evolution and energy absorption of FRP plates subjected to ballistic impact using a numerical model", *9th Int. LS-DYNA Users Conf.*, 2008.

[17] http://www.skchemicals.co.kr/kr/outside/carbon-fiber/sub1-1-3.html

[18] Cho, H.J., You, W.Y., Lee, S.J., Kim, I.G., Woo, K. and Kim, J.H., "Study on Prediction of Perforation Energy for Carbon/Epoxy Composite Laminates Subjected to High Velocity Impact using Quasi-static Perforation Equation", Proc. *2012 Asia-Pacific Int. Symposium on Aerospace Technology*, Jeju, Korea, 2012.

[19] LS-DYNA Theoretical Manual, Version-971, Livermore Software Technology Corporation, 2006.

[20] Fawaz, Z., Zheng, W. and Behdinan, K., "Numerical Simulation of Normal and Oblique Ballistic Impact on Ceramic Composite Armours," *Composite Structures*, Vol. 63, 2004, pp. 387-395.

DOI:10.1016/S0263-8223(03)00187-9

[21] Zeng, T., Fang, D. and Lu, T., "Dynamic Crushing and Impact Energy Absorption of 3D Braided Composite Tubes," *Materials Letters*, Vol. 59, 2005, pp. 1491-1496.

DOI:10.1016/j.matlet.2005.01.007

[22] Menna, C., Asprone, D., Caprino, G., Lopresto, V. and Prota, A., "Numerical Simulation of Impact Tests on GRFP Composite Laminates," *Int. J. of Impact Engineering*, Vol. 38, 2011, pp. 677-685.

DOI:10.1016/j.ijimpeng.2011.03.003

[23] Park, C.-K., Kan, C.-D., Hollowell, W.T. and Hill, S.I., "Investigation of Opportunities for Lightweight Vehicles Using Advanced Plastics and Composites," *Report No. DOT HS 811 692*, Washington, DC: National Highway Traffic Safety Administration, 2012.

[24] Hsiao, H.M. and Daniel, I.M., "Strain Rate Behavior of Composite Materials," *Composites Part B*, Vol. 29, Issue 5, 1998, pp. 521-533.

DOI:10.1016/S1359-8368(98)00008-0

[25] Gilat, A., Goldberg, R.K. and Roberts, G.D., "Experimental Study of Strain-Rate-Dependent Behavior of Carbon/Epoxy Composite," *Composites Science and Technology*, Vol. 62, 2002, pp. 1469-1476.

[26] Xiao, J.R., Gama, B.A. and Gillespie, Jr., J.W., "Progressive Damage and Delamination in Plain Weave S-2 Glass/SC-15 Composites Under Quasi-Static Punch-Shear Loading," *Composite Structures*, Vol. 78, 2007, pp. 182-196.

DOI:10.1016/j.compstruct.2005.09.001